HIGH-RESOLUTION IMAGING OF HIGH MOBILITY RATIO, IMMISCIBLE DISPLACEMENTS

Guo-Qing Tang and Anthony R. Kovscek,
Department of Petroleum Engineering, Stanford University, CA 94305

This paper was prepared for presentation at the International Symposium of the Society of Core Analysts held in Toronto, Canada, 21-25 August 2005

ABSTRACT

Immiscible, high-mobility ratio waterflood is little studied. By analogy to miscible flooding, the sweep efficiency likely depends on the distribution of heterogeneity; because the displacement is immiscible, the local displacement efficiency must be less than 1. Beyond these generalizations, there is, apparently, little or no in-situ, fine-scale (order mm^3) saturation versus time data for high mobility ratio waterflood in extensively characterized porous media. Moreover, there are (i) no theoretical underpinnings or anecdotal evidence to suggest that steady-state measurements are representative of dynamic displacement and (ii) no evidence to support the use of a less viscous oil in place of the true oil viscosity. Berea sandstone is employed to establish the physics of high mobility ratio displacement in a linear geometry. Waterfloods with mobility ratios (from 1 to 155) at various water injection rates were conducted. X-ray computed tomography (CT) is employed to visualize fluid dynamics. Three-dimensional images are constructed of in-situ water movement. In addition, steady-state relative permeability measurements establish a baseline to investigate dynamic displacement behavior. Results show that in homogeneous porous media, both water (displacing phase) injection rate and oil (displaced phase) viscosity have an obvious effect on the stability of the water front. As the oil viscosity increases, the water front becomes less stable.

INTRODUCTION

For the past half century, waterflood has accounted for 50% of oil recovered. Application of waterflood in viscous oil reservoirs is widely discounted, but for Arctic and offshore reservoirs there are perceived to be few recovery process options. The main limitations of application of waterflood to viscous oil are unfavorable, high mobility ratio and substantial injection pressure. When the mobility ratio is substantially greater than 1, viscous fingering of water through the oil phase may occur (Meurs, 1957, Benham and Olson, 1963, Gupta and Greenkorn, 1974, Hagoort, 1974, Sigmund et al., 1988, Abrams, 1975, Perking, 1957, Douglas, et al., 1958, Pavone, 1992). The most important parameter governing frontal stability is mobility ratio. Hagoort (1974) chose the ratio of fluid mobility downstream and total mobility upstream of the front to define a shock mobility ratio. The shock mobility ratio is generally less than the endpoint mobility ratio implying stability for some displacements judged unstable by endpoint mobility calculations.

The effects of high mobility ratio are manifest in both macroscopic and microscopic displacement efficiency. As the mobility ratio increases, the Buckley-Leverett frontal

advance analysis predicts that the size of the water bank upstream of the front decreases and its velocity correspondingly increases. This leads to more rapid breakthrough of water in comparison to smaller mobility ratios. Additionally, viscous fingering is promoted and, the displacement front between water and oil becomes unstable. Oil trapped by water is possibly remobilized by so a called “drag” force (Smith, 1992).

This work focuses on viscosity ratio and stability of oil displacement by water in strongly water-wet, homogeneous Berea sandstone. Clean, white mineral oils of various viscosities negate wettability variation. X-ray computed tomography (CT) scanning measures the evolution of in-situ water-phase saturation and monitors water front movement. The key questions examined: (i) Are steady-state measurements representative of the dynamic displacement of viscous oil? (ii) Can a less viscous oil be used in place of the true oil viscosity during measurement of rock flow properties? (iii) Does initial water saturation affect displacement stability? This paper proceeds by first laying out the experimental details and procedures. Then, results, discussion, and conclusions follow. Results show that the oil-water viscosity ratio and injection rate play key roles in the stability of the displacement front.

EXPERIMENTAL DETAILS

The experimental objective was to obtain high-resolution, in-situ images of high mobility ratio waterflood dynamics. The fluid system chosen was brine and white mineral oils, of various viscosities, so that oil/brine/rock (OBR) interactions are constant and the rock remains water wet. Design elements for the apparatus include: (i) a strongly water wet Berea sandstone, (ii) immiscible fluid pairs with oil/water viscosity ratios that range from roughly 1 to 155, (iii) potting the core in an aluminum holder to allow collection of X-ray CT images of in-situ, water-phase distribution, (iv) selection of water injection rates that minimize potential capillary end effects, and (v) negligible gravity forces.

A strongly water-wet Berea sandstone with a length of 52 cm and a diameter of 5.1 cm was selected. Thus, the aspect ratio for this rock is about 0.1. The average permeability to water and the porosity are 377 md and 20.5%, respectively. The core is potted in an aluminum coreholder with a wall thickness of 0.3 cm. The aluminum also serves to filter the incident X-rays, thereby improving monochromaticity, and minimizing X-ray beam hardening artifacts (e.g., Akin and Kovscek, 2003). Epoxy fills the annulus between the core and coreholder. Prior to potting, the surface of the core is coated with numerous thin layers of epoxy to seal all surfaces. Subsequent CT scans verify little to no invasion of epoxy into the core. Five pressure measurement ports were machined through the aluminum at equal intervals along the core. Including the pressure measurement at inlet, there were 6 pressure transducers (DP31, Celesco transducer products inc.) installed along the core. The core was characterized extensively, as discussed in a later section.

Exceptional care was exerted during selection of fluids. The chief concerns governing fluid selection were: (i) the rock wettability should not change from experiment to experiment and (ii) the difference between oil and brine phase CT number should as large as practical so as to monitor clearly the water advancing front during displacement. An 8% by weight NaBr brine is selected as initial water and injection water. This brine has a CT number of 469, as compared to 0 for pure water and –1000 for air. A typical oil has a

CT number of –180. The CT number is a measure of the degree of X-ray attenuation by a material and the greater the CT number the greater the attenuation. The greater the difference in fluid-phase CT numbers, the greater the resolution obtained and the smaller the error when computing fluid-phase saturation at the pore space (Akin and Kovscek, 2003). Three clean mineral oils with viscosities of 0.97 cp (n-decane), 26.7 cp (blandol), and 155 cp (drakeol) at room temperature, respectively, were selected as oil phases. Because these three oils do not contain polar oil components, such as asphaltenes and their associated resins, no wettability alteration results and the rock remains strongly water-wet, as proved by imbibition measurements.

The estimated mobility ratio utilizing endpoint water and oil relative permeability is 0.07 for water/n-decane, 2. for water/blandol, and 12 for water/drakeol. The three water/oil systems represent the full spectrum of mobility from very favorable (M<1) to unit to quite unfavorable (M>1).

Flood Rates

The oil/water/rock system is strongly water-wet and it follows that the effect of capillary forces on displacement stability and end effects should not be neglected. Based on the Rapoport-Leas analysis (Rapoport and Leas, 1953), the ratio of viscous forces to capillary forces determines the stability of displacement. This ratio is expressed as

$$N_{RL} = (\frac{\phi}{k})^{0.5} \frac{\mu_w u L}{k^*_{rw} \phi \sigma_{ow} \cos\theta} \quad (1)$$

where N_{RL} is the Rapoport-Leas number, ϕ is the porosity, k is the absolute permeability, μ_w is the water viscosity, u is the Darcy velocity, L is the length of the core, k^*_{rw} is the end-point water relative permeability, σ is water-oil interfacial tension, and θ is the contact angle. The flow rate must be large so that viscous forces overcome capillary forces, but not so large that residual oil is mobilized. The range of acceptable N_{RL} is (Lake, 1989):

$$3 < N_{RL} < 10^{-5} L (\frac{\phi}{k})^{0.5}. \quad (2)$$

For the experimental conditions here, the critical lower bound for brine injection rate is 0.14 m/d whereas the upper bound is 31 m/d. Three appropriate injection rates were selected: 0.35 m/d (q=0.5 cm^3/min), 1.05 (q=1.5 cm^3/min), and 2.11 m/d (q=3.0 cm^3/min), respectively.

The core is first saturated with brine. Oil is injected at 2 cm^3/min until water production ceases. A CT scan of the core verifies that spatially homogeneous initial water saturation is established. Brine injection to displace oil is at a constant rate from one end of the core. The oil and water are produced and collected from other end of the core. The unsteady-state displacement continues until steady-state is reached.

Imaging Protocols and Processing

The CT scanner is a fourth generation Picker 1200SX with 1200 fixed detectors and a scan angle of 398° (360° plus 38° overscan to provide redundancy). Images are collected with the tube current set to 125 mA and the energy level of the X-rays set to 135 keV.

Such high energy scans also help to minimize image artifacts. The acquisition time of one image is roughly 4 s, while the processing time is about 20 s. Images are acquired in series with processing delayed until all the desired X-ray exposures are collected. Each voxel has a dimension of 0.35 mm by 0.35 mm with a thickness of 5 mm. The coreholder is fixed horizontally on a positioning system (Compumotor, RP 240, Parker-Hamnifan) that allows precision repeat translation of the coreholder (±0.01 mm). Cylindrical volume sections are monitored at 2 to 5 cm intervals along the central axis of the core.

The raw CT images collected are processed to obtain the porosity and the aqueous phase water saturation. Voxel by voxel measurements of CT number are subtracted as discussed next. Porosity is obtained from CT images as

$$\phi = \frac{CT_{wr} - CT_{ar}}{CT_w - CT_a}, \tag{3}$$

where CT is the voxel by voxel measurement of X-ray attenuation, the subscripts *wr* and *ar* refer to water-filled and air-filled rock respectively, and the subscripts *w* and *o* refer to bulk water and air phases, respectively.

The matrix of water saturation, S_w, presented in each cross-sectional image is computed as

$$S_w = \frac{CT_{wr} - CT_{owr}}{\phi(CT_w - CT_o)} \tag{4}$$

where ϕ is the independently measured porosity of a voxel and the subscript *owr* refers to rock containing oil and water phases. The average water saturation at a particular axial location was obtained by averaging the voxel by voxel measurements of water saturation of each cross section. The average initial water saturation of the core was obtained by averaging the cross sectional measurements of the aqueous phase saturation. **Figure 1** is a graphical illustration of the experimental and CT-imaging protocol. With the CT-derived images of water saturation versus time, the water advancing front versus time is established. Thus, the displacement front is classified as stable or not stable. Combined with oil and water production and pressure data, we establish the oil recovery, water-cut, and dynamic relative permeability at each displacement condition.

CORE CHARACTERIZATION

To characterize heterogeneity within the core, the porosity and permeability distribution in both areal and axial directions was measured with the aid of the CT scanner. The core was scanned under dry condition and fully water-filled conditions. In total 26 porosity CT-images along the axial direction from inlet to outlet were measured. **Figure 2a** presents one of the cross-sectional images. Light shading represents high porosity and dark shading represents low porosity. The range of porosity measurements is extremely narrow and the porosity within a cross section is uniformly distributed. With the 26 porosity-CT images, we reconstructed a 3D-porosity image illustrated in **Figure 2b**. Evidently, the porosity distribution along the axial direction is also uniform. Note that the core is cylindrical and the square cross section in Fig.2 is simply for ease of presentation. The square is 3.6 cm on a side.

In order to measure the permeability distribution, 0.5% NaCl brine was used as the initial water that saturates (S_w = 1) the core. An 8% NaBr brine was then injected to displace miscibly the NaCl brine. The CT numbers for the two brines are 18 for 0.5% NaCl brine and 469 for 8% NaBr brine. Thus we trace the injected brine by CT-scanning the coreholder. The same 26 locations for porosity measurements are again used. The time for the front to move from one location to following locations is also measured. Thereafter, the permeability distribution is estimated in both areal and axial directions using an approach proposed by Withjack (1988). The core is assumed to be composed of a set of streamtubes with negligible variation of cross sectional area along the length of each tube. The permeability of each voxel is calculated as

$$k_1 = \frac{k_{average} A_T}{A(1 + \frac{\phi_2 t_1}{\phi_1 t_2} + \frac{\phi_3 t_1}{\phi_1 t_3} + ... + \frac{\phi_n t_1}{\phi_1 t_n})} \quad (5)$$

where $k_{average}$ is the average, independently measured permeability, ϕ_i is the individual streamtube porosity, t_i is the time for 8% NaBr brine flow along the given length of the core, A is the total cross-sectional area, and A_T is the tube cross-section area. The permeability of any other voxel is found as

$$\frac{k_n}{k_1} = \frac{\phi_n t_1}{\phi_1 t_n} \quad (6)$$

Figure 3 presents the reconstructed 3D-permeability distribution. There are low permeability values measured at the outer edge of the core. They are caused by minor intrusion of epoxy. Even a superficial study of the permeability distribution teaches that this core is quite homogeneous. The variance of the permeability is 0.001.

RESULTS

Numerous experiments were conducted. **Figure 4** presents a representative suite of CT-images that display features of the water advancing front for different oil/water systems at the same injection rate. The saturation scale is given on the right. White shading represents high water saturation and black shading represents the initial water saturation of about 29-31%. Water volume injected is presented as pore volumes, PVI. The dimensionless axial location for these images is X_D=0.04 (close to the inlet) and the injection rate is 0.35 m/d. An increase in the fraction of images that are lightly shaded represents water invasion. For an M of 0.07, as given in **Figure 4a**, the white color increases uniformly and quickly as the displacement front reaches a particular axial position. This behavior indicates that the water flood is uniform and stable. The displacement is piston-like and quite effective. Sensibly, there is no oil flowing behind the advancing front. Similar behavior is obtained in all cross sections.

The mobility ratio was then increased to 2. The core was evacuated, resaturated with water, brought to initial conditions, and a new displacement was begun. **Figure 4b**, summarizes results. The white shading appearing in the cross-sectional images is not uniform. About 40-50% of the cross-sectional area is swept by water at 0.01 PVI. The water swept area upstream of the front gradually increases with time as evidenced by the

increase in white shading. At 0.0226 PVI, about 80% of the cross-sectional area is swept by water at this axial location.

Next, the mobility ratio is increased to 12, the core is initialized, and water is injected. In this case, the displacement is quite unstable, **Figure 4c**. The water saturation pattern is not uniform. Small white spots of large water saturation appear randomly at early time throughout the cross-sectional area. These indicate that the water front is not sharp and is dispersed. Viscous fingering is obvious. As the water injection continues, the regions with large water saturation gradually expand and merge.

Reconstructed 3D images of the distribution of water saturation for all mobility ratios give a more direct view of the pattern of advancing water, as shown in **Figure 5**. The water advancing front for the favorable mobility ratio of 0.07 is sharp and stable; the displacement is typically piston-like. As the mobility ratio increases to 2 and further to 12, the displacement gradually switches to non-piston like. A dispersed front and bypassed rock volumes are observed.

The injection rate was also varied to ascertain if it had an effect on displacement stability. **Figure 6a** summarizes, via a set of water saturation CT-images, the effect of rate on displacement at two different mobility ratios, 0.07 and 2. The location of the cross sections is X_D equal to 0.46. For mobility ratio of 0.07, an increase in injection rate from 0.35 to 1.05 m/d does not change appreciably the shape of the water advancing front. The displacement remains piston-like, water invades uniformly, and the entire cross-section is swept by water. For mobility ratio of 2, an increase in injection rate from 0.35 to 1.05 m/d shows a significant effect on the shape of the front. At greater rate, the water front splits into two fingers. Some regions are bypassed leaving behind area that is yet to be swept by water. This behavior is observed for the entire core from inlet to outlet. **Figure 6b** displays the reconstructed 3D water saturation profile. Visually, the water advancing front is more dispersed at the greater water injection rate of 1.05 m/d.

When the injection rate is increased further to 2.11 m/d, similar behavior is observed for each mobility ratio. The displacement with the mobility ratio of 0.07 remains stable and piston-like. For mobility ratios of 2 and 12, the transient displacement is characterized as non-piston-like and the front is more dispersed for greater M. Some oil is left behind the front that is produced at high water fractional flows. The images are not presented here for sake of brevity.

We also studied the effect of initial water saturation on stability of the water advancing front. For M equal to 0.07 and injection rate of 0.35 m/d, the water front shows a surprisingly dispersed pattern at S_{wi}=0, not shown. The water bypasses some oil and water fingers through the middle of the cross-section. The displacement is not piston-like as observed for the core at S_{wi}= 33%. When the mobility is increased to 12, the viscous fingering becomes substantially more aggressive at S_{wi}=0, as shown in **Figure 7**. A thin and long finger is persistently observed with time from inlet to outlet. This result indicates that the presence of initial water saturation plays a stabilizing role.

One-Dimensional Saturation Profiles

One-dimensional water saturation profiles were computed from the CT-image data, as presented in **Figure 8**, to summarize the effect of mobility ratio. For the stable

displacement of M equal to 0.07, the dynamic, one-dimensional water saturation profile is piston-like as discussed above. The saturation front is steep and moves stably toward the outlet. The mobility of the oil behind the front is sensibly zero. The water saturation across the front varies from S_{wi} to $1-S_{or}$. No oil production following breakthrough is measured, **Fig. 9a** and **10a**. For the displacement with M equal to 2, the saturation front is similar in some respects to that for M equal to 0.07. There is, however, mobile oil in the swept zone, indicating that the displacement is not complete and that the bypassed oil is still mobile. As water injection continues, this oil is swept out at high water fractional flow. The displacement front appears to become slightly more dispersed as it approaches the outlet, For the largest mobility ratio of 12, the water advancing front is quite dispersed at all time levels. No evidence of a stable front is observed in the entire displacement process. The viscous fingering, captured above in the CT images, results in irregularly shaped displacement fronts and early water breakthrough. An important feature is that the water saturation continues to increase upstream of the displacement front.

The effect of injection rate on saturation profile is studied. For the favorable mobility ratio of 0.07, the front shape does not change as rate is increased. When M equals 12, the saturation profiles reflect a significantly dispersed front as injection velocity increases. The oil left behind the water front is continuously displaced by the water injected at late time. Reduction in initial water saturation gives similar results that are not shown for reasons of brevity.

In summary, the dynamic water saturation profiles show: (1) increased mobility ratio results in an increasingly unstable displacement: (2) increased injection velocity does not affect frontal stability for favorable mobility ratio displacements; (3) increased injection rate decreases frontal stability for unfavorable mobility ratio displacements; and (4) a decrease in initial water saturation makes viscous fingering of water through oil more significant.

Oil Recovery and Water Cut

Recall that initial water saturation is around 27-33% in all cases whereas the injection rates are 0.35, 1.05 and 2.11 m/d, respectively. **Figure 9** shows the oil recovery curves for the three oil/water systems at three different rates. Firstly, the recovery for M equal to 0.07 does not change with injection rate. The recovery curves are identical. There is a slight difference among recovery curves for M equal to 2. The water breakthrough for an injection velocity of 2.11 m/d is about 0.03 PV earlier than the other experiments. For mobility ratio of 12, the breakthrough oil recovery is significantly reduced from 0.37 to 0.27 OOIP. The water breakthrough time is about 0.08 PV earlier as the injection velocity increases to 2.11 m/d. Secondly, the breakthrough oil recovery decreases with increase in mobility ratio. Recovery is about 0.47 OOIP for M=0.07, 0.44 OOIP for M=2 and 0.28-0.38 OOIP for M=12. This behavior suggests that the breakthrough oil recovery (or time) is a function of both mobility ratio and injection rate. Thirdly, the ultimate recovery of 0.46-0.47 OOIP is the same for all three oil/water systems. The recovery rate, however, is not the same. For the mobility ratio of 0.07, it takes 0.3 PV of water injection to reach

final oil recovery. For M equal to 2, it takes 1.2-1.5 PV of water injection and for M equal to 12, it takes 2 to 4 PV of water injection.

Figure 10 presents the water cut measured at the outlet of the core. Similar to oil recovery behavior, the water-cut is not influenced by water injection rate when M is 0.07. When the mobility ratio increases to 2, the water cut shows a response to increase in injection velocity from 1.05 to 2.11 m/d and earlier breakthrough. For M equal to 12, the water cut is strongly influenced by injection rate and the water cut increases slowly with injection rate. This behavior results in early water breakthrough that leaves a great amount of oil behind the water front.

Steady-State Relative Permeability

Experiments were designed carefully to obviate the effect of capillary forces, wettability alteration, and heterogeneity. The role of mobility ratio on macroscopic and microscopic displacement efficiency has been the focus of study. The greater the mobility ratio, the less stable the advancing front. To arrive at an explanation for this behavior, we measured the steady-state relative permeability for the three water/oil systems, as presented in **Figure 11a.** The measurement procedure is standard (Honarpour et al, 1986). Apparently, the oil relative permeability for the most viscous oil (μ_o=155 cp) differs from the other two oils, revealing an effect of viscosity ratio on relative permeability. The role of capillary pressure on measured relative permeability is discussed elsewhere (Kokkedee, 1996; Mas, 1997)

To analyze the effect of viscosity ratio on the stability of displacement, the one-dimensional, dispersion-free, Buckley-Leverett / fractional flow framework is used (Lake, 1989). **Figures 11b** and **11c** compare fractional flow behavior of the viscous oil/water system. As the oil viscosity increases from 27.6 cp to 155 cp: (1) Figure 11b indicates that the shock saturation decreases from 0.57 to 0.52, given immobile initial water saturation; (2) the shock velocity ($\Delta f_w/\Delta S_w$) on Figure 11c decreases slightly from 4.1 to 3.75.

The shock mobility is defined as the ratio of the total mobility at shock water saturation to that at initial water saturation (Hagoort, 1974, Riaz and Tchelepi, 2004). It is used to judge the stability of displacement. When the shock mobility ratio is less than 1, the displacement is stable; when it is greater 1, the displacement is unstable. For the system with oil viscosity of 0.93 cp, the calculated shock mobility is 0.070. As a result, the displacement is predicted to be absolutely stable, as observed experimentally. For the system with oil viscosity of 27.6 cp, the calculated shock mobility is 0.83 and is of order 1. Ideally, the displacement should be unconditionally stable. The experimental results show displacement is largely stable at low injection velocity, but becomes less stable and less piston-like as the injection velocity increases. The injection velocity plays a role on the stability (Hagoort, 1974, Riaz and Tchelepi, 2004). For the system with oil viscosity of 155 cp, the shock mobility is about 2.2. This value is substantially greater than 1 and the displacement is not stable at any injection velocity, as observed experimentally.

CONCLUSIONS

This study leads to several conclusions of practical significance. First, relative permeability is function of viscosity ratio for unstable, high-mobility ratio steady-state displacements. Lower viscosity oil phases cannot be substituted for more viscous nonwetting phases during characterization of relative permeability or multiphase flow properties. Second, the viscous instabilities measured are benign in many senses. Viscous fingers do form, but they do not lead the displacement front by significant distances. Significant oil is not trapped and left stranded by the formation of viscous fingers. Mobile oil behind the displacement front is produced, albeit by continued water injection at an increasing water cut. Third, in concert with the second conclusion, the residual oil saturation is sensibly independent of oil viscosity. These results suggest that displacement efficiency for high mobility ratio waterflood is largely characterized by one-dimensional Buckley-Leverett displacement calculations. The impact of heterogeneity on larger-scale displacements is well handled by conventional techniques that characterize the spatial distribution of heterogeneity. Fourth, the so-called shock mobility ratio is predictive in determining the stability of a displacement. When the shock mobility ratio is greater than 1, as determined by steady-state relative permeability, the displacement is unstable. Hence, steady-state measurements are, in a sense, predictive of the dynamics of high mobility ratio waterflooding. Finally, large injection rate and low initial water saturation generally lead to non stable displacement when the mobility ratio is 1 or greater.

ACKNOWLEDGEMENT

The authors thank A. Raiz and H. Tchelepi of Stanford University as well as Viet Hoang, M. Kumar, and C. Satik of Chevron for helpful discussions. Financial support was provided by Chevron and the SUPRI-A Industrial Affiliates.

REFERENCES

1. Abrams, A., “The influence of fluid viscosity, interfacial tension, and flow rate on residual oil saturation left by waterflood,” SPEJ, (Oct, 1975), 437-447.
2. Akin, S. and A. R. Kovscek, “Computerized tomography in petroleum engineering research,” in Applications of computerized X-ray tomography in geology and related domains, Special Publication, Geological Society, London, 215, (2003), 23-38.
3. Benham, A. L., and Olson, R. W., “A Model Study of Viscous Fingering,” Trans., AIME 228 (1963), 138-144.
4. Douglas Jr.,J., Blair, P. M., and Wagner, R. J., “Calculation of Linear waterflood behavior including the effects of capillary pressure,” Petroleum Transactions, AIME, Vol. 213, (1958), pp.103-112.
5. Gupta, S. P. and Greenkorn, R. A., “An Experimental Study of Immiscible Displacement with an Unfavorable Mobility Ratio in Porous Media,” Water Resources Res., (April 1974), 10, No.2, 371-74.
6. Hagoort, J., "Displacement Stability of Water Drives in Water-Wet Connate-Water-Bearing Reservoirs," Trans. AIME, Vol. 257 (1974), 63-74.

7. Honarpour, M., Koederitz, L., and Harvey, A. H., “Relative permeability of petroleum reservoirs,” CRC Press Inc., Boca Raton, FL (1989).
8. Kokkedee, J.A., Boom, W., Frens A.M. and Maas, J.G., "Improved Special Core Analysis: Scope for a Reduced Residual Oil Saturation," SCA 1996-01, Proceedings of the Intl. SCA Symposium, Montpelier, France, Sept. 11-13, 1996.
9. Lake, L W. “Enhanced Oil Recovery,” Prentice-Hall Inc, Englewood Cliffs, New Jersey. 1989. 146.
10. Maas, J. G. and Schulte, A.M. "Computer Simulation of Special Core Analysis (SCAL) Flow Experiments Shared on the Internet," SCA 1997-19, Proceedings of the Intl. SCA Symposium, Calgary, AB Canada, Sept. 8-10, 1997.
11. Meurs, P. Van, “The use of transparent three-dimensional models for studying the mechanism of flow processes in oil reservoirs,” Petroleum Transactions, AIME Vol. 210 (1957) , 295-301.
12. Pavone, D., “Observation and correlations for immiscible viscous-fingering experiments,” SPE Reservoir Engineering, (May 1992), 187-192.
13. Perking, Jr., F. M., 1957, “An investigation of the role of capillary forces in laboratory water floods,” Vol. 210, 409-411.
14. Rapoport, L.A. and Leas, W. J., “Properties of linear waterfloods,” Petroleum Transactions, AIME, Vol. 198, (1953) 139-148.
15. Riaz, A. and Tchelepi, H., “Linear stability analysis of immiscible displacements with capillary dispersion,” Physics of Fluids, Vol. 16, No. 12, 4727-4737.
16. Sigmund, P., Sharma, H., Sheldon, D., and Aziz, K. “Rate dependence of unstable waterfloods,” SPE Reservoir Engineering, (May1988), 401-409.
17. Smith, G. E., “Waterflooding heavy oils,” paper SPE 24367 presented at the SPE Rock mountain regional meeting held in Casper, WY., May 18-21, 1992.
18. Withjack, E.M, “Computed tomography for rock property determination and fluid flow visualization,” SPE Formation Evaluation. 3 (1988), 694-704.

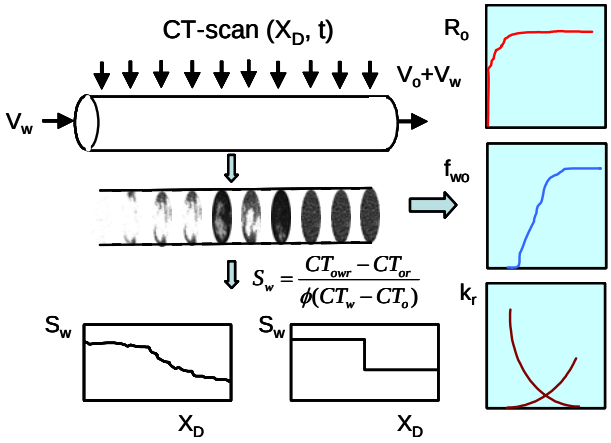

Figure 1. Experimental-protocol.

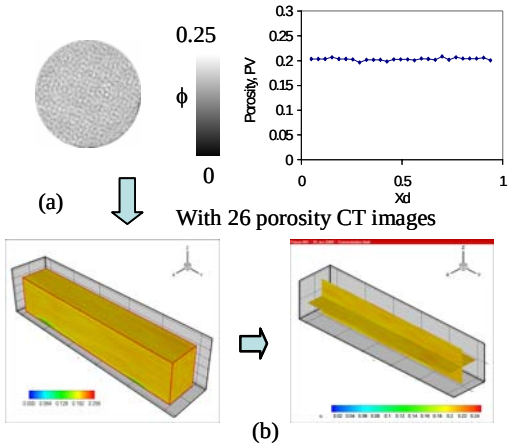

Figure 2. Porosity distribution: (a) CT-image and ϕ versus X_D, (b) 3D porosity image

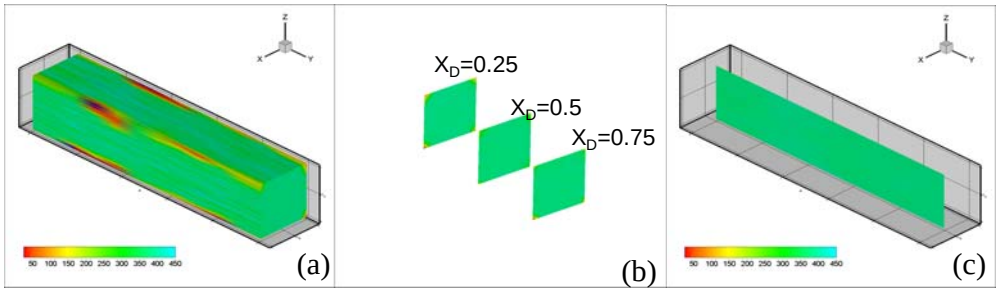

Figure 3. Permeability distribution: (a) 3D, (b) 2D cross-section, (c) 2D along the axial distance

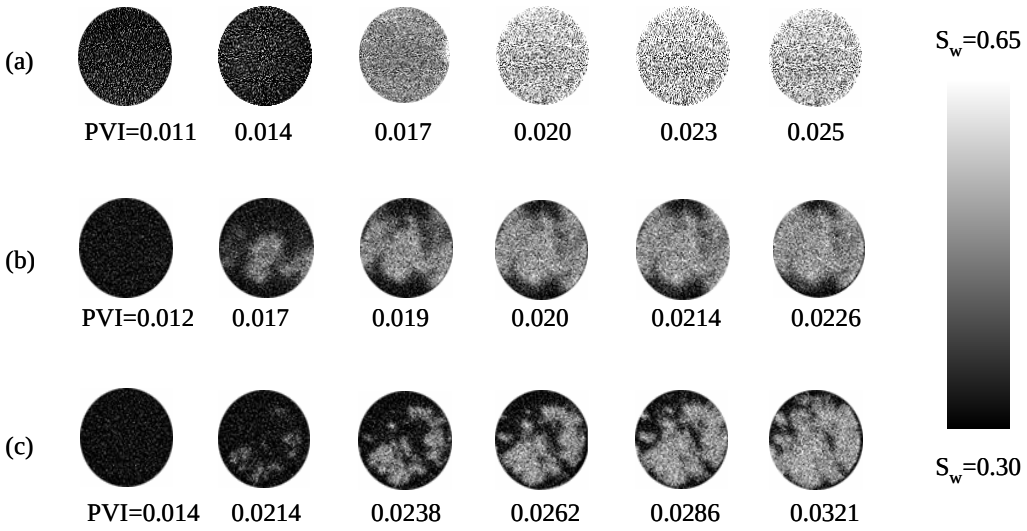

Figure 4. Water saturation CT-images versus time at X_D=0.04: viscosity effect. Brine injection rate=0.35 m/d: (a) M=0.07, (b) M=2, (c) M=12

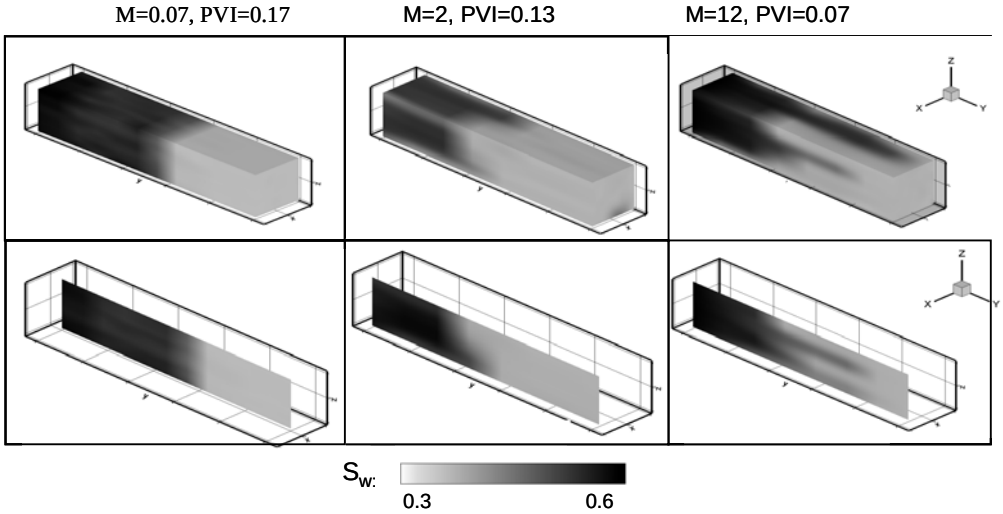

Figure 5. Reconstructed 3D water saturation images: mobility ratio effect (U=0.35 m/d)

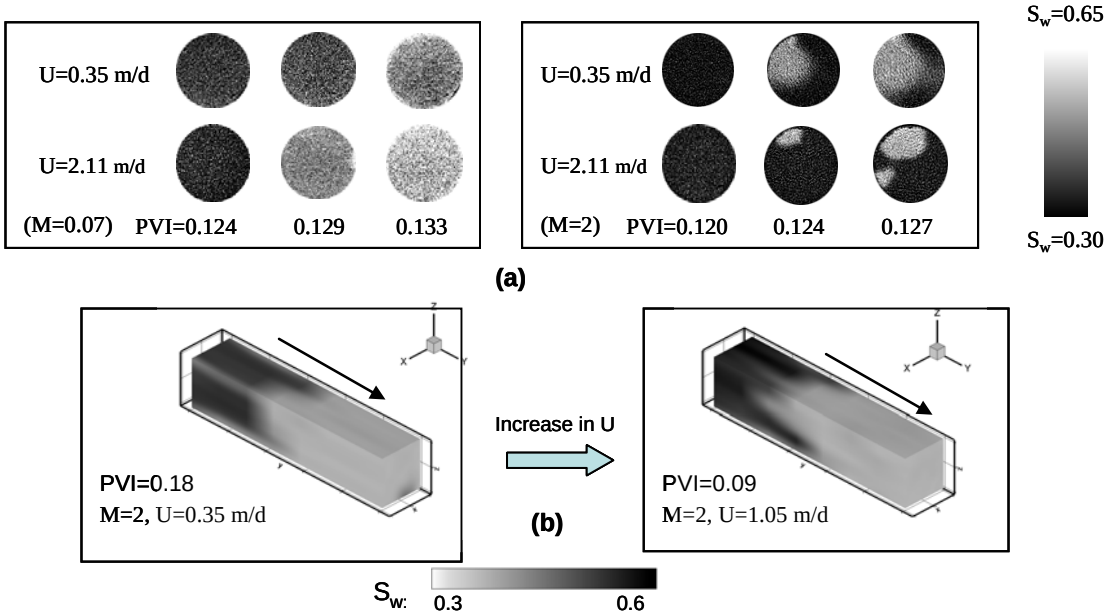

Figure 6. Effect of injection rate on water advancing front stability: (a) S_w CT-images, (b) reconstructed S_w images

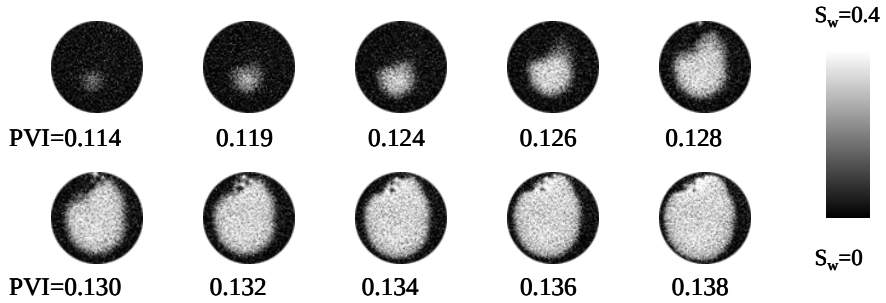

Figure 7. Unstable displacement at zero initial water saturation: X_D=0.25, M=12, U=0.35 m/d

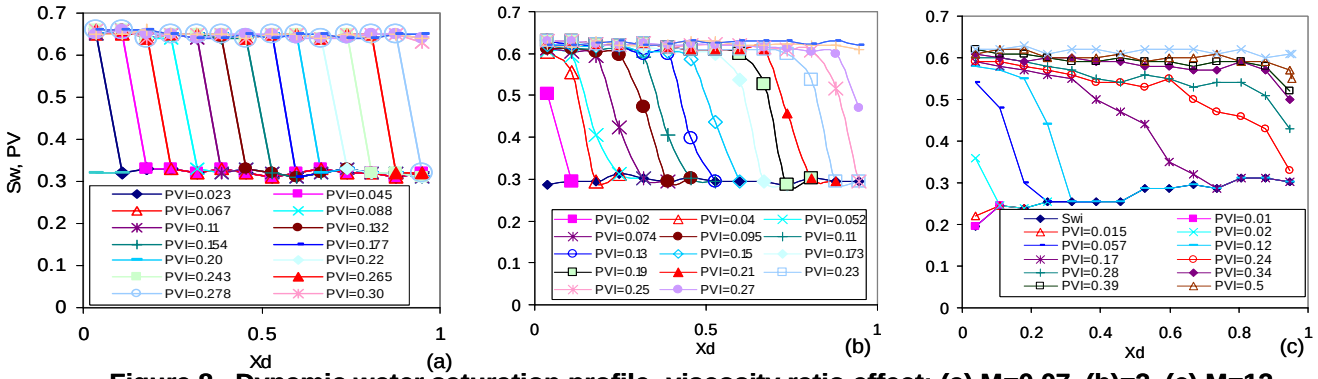

Figure 8. Dynamic water saturation profile- viscosity ratio effect: (a) M=0.07, (b)=2, (c) M=12

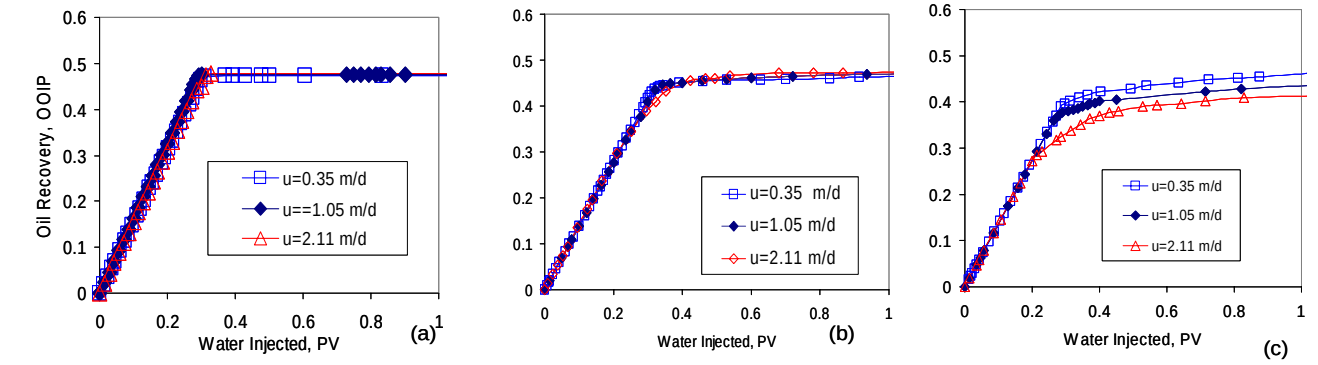

Figure 9. Oil recovery curves: (a) M=0.07, (b)=2, (c) M=12

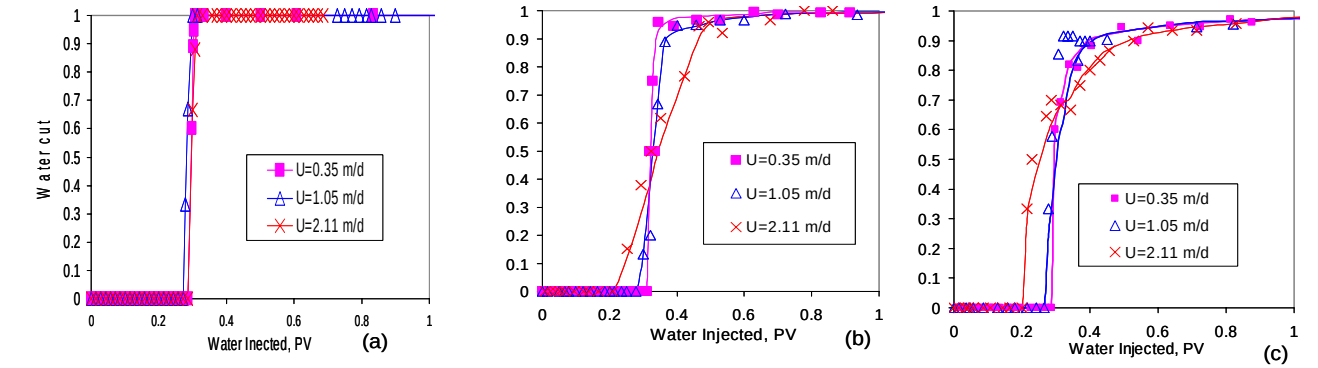

Figure 10. Producing water-cut curves: (a) M=0.07, (b)=2, (c) M=12

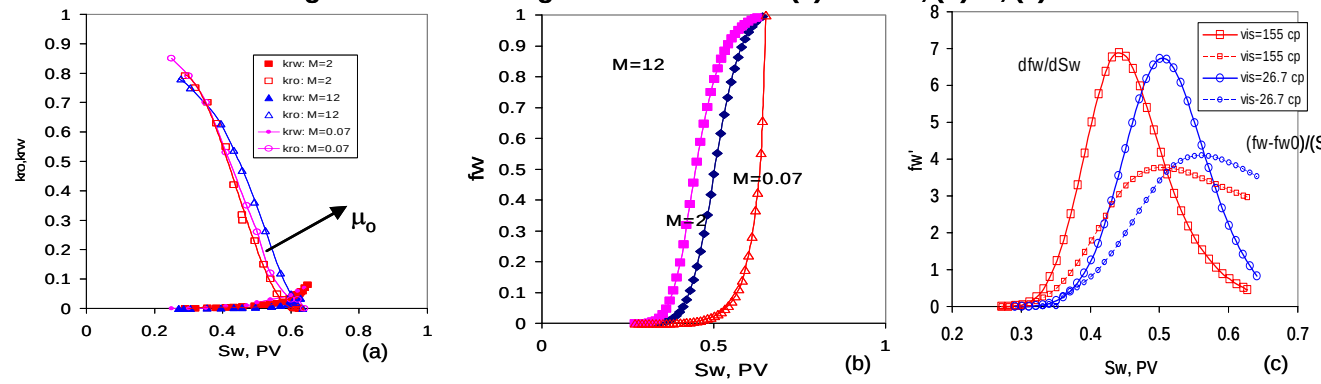

Figure 11. One dimensional Buckley-Leverett analytical solution: (a) relative permeability, (b) water fractional flow, (c) effect of oil viscosity on shock saturation